

## Article

# Photoluminescence and Temperature Sensing Properties of Bi<sup>3+</sup>/Sm<sup>3+</sup> Co-Doped La<sub>2</sub>MgSnO<sub>6</sub> Phosphor for Optical Thermometer

Qingliang Xu <sup>1</sup>, Wanqing Qian <sup>1</sup>, Raz Muhammad <sup>2,\*</sup> , Xinhua Chen <sup>1</sup>, Xueqing Yu <sup>1,\*</sup> and Kaixin Song <sup>1,\*</sup> 

<sup>1</sup> College of Electronics Information, Hangzhou Dianzi University, Hangzhou 310018, China; xqlhero@163.com (Q.X.); qyuzuru@163.com (W.Q.); chancy\_hua@163.com (X.C.)

<sup>2</sup> Department of Physics, Garden Campus, Abdul Wali Khan University Mardan, Mardan 23200, Pakistan

\* Correspondence: raz@awkum.edu.pk (R.M.); xqyu@hdu.edu.cn (X.Y.); kxsong@hdu.edu.cn (K.S.)

**Abstract:** The optical temperature sensor utilizing the fluorescence intensity ratio (FIR) has garnered significant attention in the past few years due to its rapid response, robust anti-interference capability, remote control feature, and other advantages. In this study, the high-temperature solid-phase approach was used to fabricate a variety of double perovskite-structured La<sub>2</sub>MgSnO<sub>6</sub>: Bi<sup>3+</sup>, Sm<sup>3+</sup> (LMS: Bi<sup>3+</sup>, Sm<sup>3+</sup>) phosphors. The Rietveld refinement data of XRD and the Gaussian fitting of the emission peak of LMS: 0.02Bi<sup>3+</sup> phosphor indicated Bi<sup>3+</sup> occupies three lattice sites. The calculation and analysis of average lifetime and energy transfer efficiency substantiated the presence of energy transfer from Bi<sup>3+</sup> to Sm<sup>3+</sup>, with a transfer efficiency of up to 59.07%. The emission intensity of LMS: 0.02Bi<sup>3+</sup>, 0.05Sm<sup>3+</sup> at 403 K maintains 50.2% at the condition of room temperature. The FIR fitting and calculation demonstrated that LMS: 0.02Bi<sup>3+</sup>, 0.05Sm<sup>3+</sup> phosphor possessed good optical temperature sensitivity, with a maximum absolute sensitivity S<sub>a-max</sub> of 0.0055 K<sup>-1</sup> and a maximum relative sensitivity S<sub>r-max</sub> of 0.88% K<sup>-1</sup>, demonstrating its valuable potential applications for optical temperature sensors.

**Keywords:** phosphors; fluorescence; sensitivity; temperature sensors



**Citation:** Xu, Q.; Qian, W.; Muhammad, R.; Chen, X.; Yu, X.; Song, K. Photoluminescence and Temperature Sensing Properties of Bi<sup>3+</sup>/Sm<sup>3+</sup> Co-Doped La<sub>2</sub>MgSnO<sub>6</sub> Phosphor for Optical Thermometer. *Crystals* **2023**, *13*, 991. <https://doi.org/10.3390/cryst13070991>

Academic Editor: Kil Sik Min

Received: 31 May 2023

Revised: 16 June 2023

Accepted: 19 June 2023

Published: 21 June 2023



**Copyright:** © 2023 by the authors. Licensee MDPI, Basel, Switzerland. This article is an open access article distributed under the terms and conditions of the Creative Commons Attribution (CC BY) license (<https://creativecommons.org/licenses/by/4.0/>).

## 1. Introduction

The application of phosphors is no longer limited to the field of lighting, but also widely used in non-contact temperature sensors, fingerprint recognition, night vision detection, etc. [1–3] Compared to general contact temperature sensors, non-contact optical temperature sensors have the advantages of fast response, strong corrosion resistance, and remote control [4]. The optical temperature sensors utilize the linear discrepancy in the thermal stability of two luminescent ions in the matrix. Researchers have prepared a variety of phosphors for non-contact temperature sensors and obtained good experimental parameters in relative sensitivity and sensitivity [4,5]. For example, Sinha et al. [5] prepared the dual emission phosphors CaMoO<sub>4</sub>: Er<sup>3+</sup>, Yb<sup>3+</sup> with a high sensitivity of 7.21 × 10<sup>-3</sup> K<sup>-1</sup> in the high-temperature range of 535–760 K. Wei [6] et al. synthesized the SrY<sub>2</sub>O<sub>4</sub>: Bi<sup>3+</sup>, Eu<sup>3+</sup> phosphors, calculating a relative sensitivity of 0.86% K<sup>-1</sup> at 433 K and an absolute sensitivity of 0.0433K<sup>-1</sup> at 563 K by opposite temperature dependence and corresponding fluorescence ratios for the fluorescence intensity of Bi<sup>3+</sup> and Eu<sup>3+</sup>. A higher sensitivity is a key factor for non-contact fluorescent temperature sensors; therefore, a good matrix may be an intrinsic factor in improving its sensitivity when applied to temperature sensors. The energy transfer process that occurs in dual-emitting phosphors applied as temperature sensors is brought on by the sensitizer's excitation energy being transmitted to the activator. For example, Pankratov [7] et al. synthesized the LaPO<sub>4</sub>: Ce<sup>3+</sup>, Tb<sup>3+</sup> phosphor, proposing two novel models for the energy transfer from Ce<sup>3+</sup> to Tb<sup>3+</sup> in LaPO<sub>4</sub>. Van [8] et al. prepared the

$\text{LiYF}_4$ :  $\text{Pr}^{3+}$ ,  $\text{Yb}^{3+}$  phosphor, proving that the dominant energy transfer is caused by cross-relaxation between  $\text{Pr}^{3+}$  and  $\text{Yb}^{3+}$ . Over the past few years, lots of double-layer perovskite phosphors with an  $\text{A}_2\text{BB}'\text{O}_6$  structure have been reported, for instance,  $\text{La}_2\text{MgTiO}_6$ :  $\text{Sm}^{3+}$ ,  $\text{Eu}^{3+}$ ,  $\text{Gd}_2\text{MgTiO}_6$ :  $\text{Bi}^{3+}$ ,  $\text{Mn}^{4+}$ ,  $\text{Gd}_2\text{ZnTiO}_6$ :  $\text{Bi}^{3+}$ ,  $\text{Y}_2\text{MgTiO}_6$ :  $\text{Mn}^{4+}$ , and  $\text{La}_2\text{MgGeO}_6$ :  $\text{Bi}^{3+}$ ,  $\text{Sm}^{3+}$ . [9–13] The stannate compound  $\text{La}_2\text{MgSnO}_6$  with a double perovskite structure makes a good host due to the favorable lattice sites for Mn, Cr, and Bi ions, etc. For instance, Lu [14] et al. developed the  $\text{La}_2\text{CaSnO}_6/\text{La}_2\text{MgSnO}_6$ :  $\text{Mn}^{4+}$  phosphor with outstanding optical performance; Wu [15] et al. synthesized the  $\text{LaMg}_{0.5}(\text{SnGe})_{0.5}\text{O}_3$ :  $\text{Cr}^{3+}$  phosphor, by adding  $\text{Ge}^{4+}$ , calculating its luminous intensity has increased by 1.6 times and the intensity at 150 °C is approximately 80% of the ambient temperature. The results mentioned above suggest the  $\text{La}_2\text{MgSnO}_6$  is a fascinating host matrix.

This work prepared stannate phosphors  $\text{La}_2\text{MgSnO}_6$ :  $x\text{Bi}^{3+}$  ( $x = 0.01, 0.02, 0.04, 0.06, 0.08$ , LMS:  $x\text{Bi}^{3+}$ ),  $\text{La}_2\text{MgSnO}_6$ :  $y\text{Sm}^{3+}$  ( $y = 0.01, 0.03, 0.05, 0.07, 0.09$ , LMS:  $y\text{Sm}^{3+}$ ), and  $\text{La}_2\text{MgSnO}_6$ :  $0.02\text{Bi}^{3+}$ ,  $y\text{Sm}^{3+}$  ( $y = 0.01, 0.03, 0.05, 0.07, 0.09, 0.11$ , LMS:  $0.02\text{Bi}^{3+}$ ,  $y\text{Sm}^{3+}$ ) employing the conventional high-temperature solid-state strategy. The XRD diffraction pattern showed that the sample's diffraction peaks closely matched those of the reference card. By refining the XRD of the sample, corresponding to unit cell parameters and bond length information were obtained, and the perovskite "tolerance factor" was calculated. The relationship between the "tolerance factor" and the fluorescence spectrum was further explored. According to the photoluminescence spectrum, the luminescence intensity of LMS:  $x\text{Bi}^{3+}$  fluctuates as the  $\text{Bi}^{3+}$  concentration increases. By analyzing the emission spectra of LMS:  $0.02\text{Bi}^{3+}$ ,  $y\text{Sm}^{3+}$ , the basis for energy transfer between  $\text{Bi}^{3+}$  and  $\text{Sm}^{3+}$  could be found. In addition, thermal quenching reasons and thermal activation energy calculations were conducted for the thermal stability under co-doping conditions.

## 2. Experimental

$\text{La}_2\text{MgSnO}_6$ :  $x\text{Bi}^{3+}$  ( $x = 0.01, 0.02, 0.04, 0.06, 0.08$ ),  $\text{La}_2\text{MgSnO}_6$ :  $y\text{Sm}^{3+}$  ( $y = 0.01, 0.03, 0.05, 0.07, 0.09$ ), and  $\text{La}_2\text{MgSnO}_6$ :  $0.02\text{Bi}^{3+}$ ,  $y\text{Sm}^{3+}$  ( $y = 0.01, 0.03, 0.05, 0.07, 0.09$ ) phosphors were synthesized through conventional high-temperature solid-state reaction. Using  $\text{La}_2\text{O}_3$  (99.99%, Aladdin),  $\text{MgO}$  (99.99%, Aladdin),  $\text{SnO}_2$  (99.99%, Aladdin),  $\text{Bi}_2\text{O}_3$  (99.9%, Aladdin), and  $\text{Sm}_2\text{O}_3$  (99.99%, Aladdin) as raw materials, we weighed them stoichiometrically. The mixtures were thoroughly ground in the agate mortar. After that, the mixtures were put in an alumina crucible and fired for 10 h in a tube furnace to 1450 °C. The samples were ground into fine powders after reaching room temperature in preparation for a series of tests.

The X-ray diffractometer (Rigaku, Ultima IV, Tokyo, Japan) with Cu–K $\alpha$  radiation was used to record the samples' X-ray diffraction patterns. The scanning electron microscope (SEM) measurements were made on the samples' micromorphology and elemental composition using a Hitachi SU8010 (Chiyoda City, Tokyo, Japan). The photoluminescence (PL) and photoluminescence excitation (PLE) spectra, fluorescence decay curve, and temperature-dependent emission spectra of samples were determined using the FLS980 (Edinburgh, UK) fluorescence spectrophotometer.

## 3. Results and Discussion

The LMS is the standard double perovskite structure of  $\text{A}_2\text{BB}'\text{O}_6$  with a monoclinic system P21/n space group with sites A, B, and B' filled by La, Mg, and Sn, respectively. Figure 1a shows the schematic diagram of its crystal structure, in which Mg and Sn form  $\text{MgO}_6$  and  $\text{SnO}_6$  octahedra with six oxygen atoms, respectively, and Mg has two sites:  $\text{Mg}_1$  and  $\text{Mg}_2$  in the crystal structure.  $\text{Mg}_2$  and Sn occupy the same site. In addition, the vertex O atoms of the octahedra of  $\text{Mg}_1\text{O}_6$  and  $\text{Mg}_2/\text{SnO}_6$  are shared, and the two ligands are arranged alternately to build a structure layer with long-range order. The La atoms and seven oxygen atoms form a  $\text{LaO}_7$  decahedron embedded in the middle of the structure layer, forming a double perovskite structure of the LMS. The Rietveld refinement result of LMS is shown in Figure 1b and Table 1.

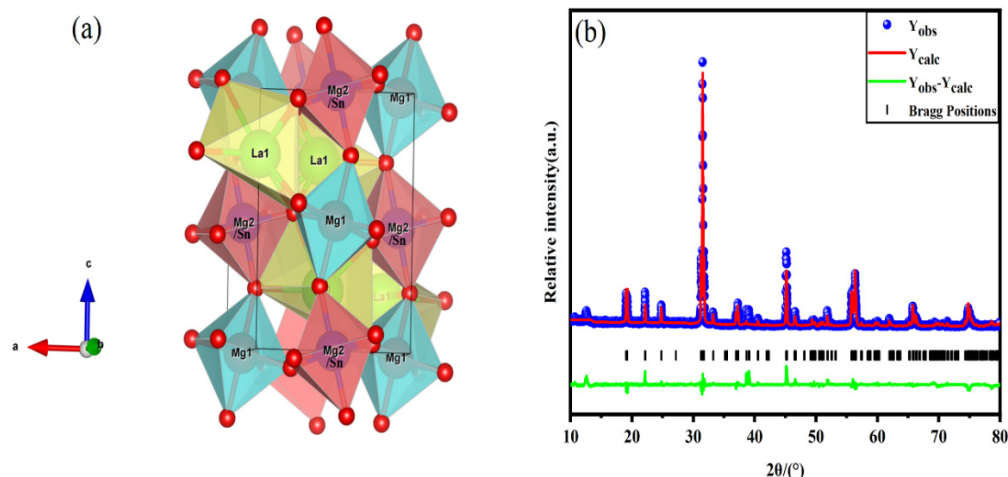


**Figure 1.** (a) Schematic diagram of LMS crystal structure; (b) refinement result of LMS.

**Table 1.** Cell parameters and refined data of LMS phosphor.

Formula	LMS
Space group	$P2_1/n$
Cell parameter (Å)	$a = 5.6362, b = 5.7228, c = 8.01927$
Volume (Å <sup>3</sup> )	258.66
Structure type	Double perovskite
$R_{wp}$ (%)	9.67
$R_p$ (%)	6.02
$\chi^2$ (%)	2.48

Figure 2 gives the XRD patterns of LMS:  $x\text{Bi}^{3+}, 0.03\text{Sm}^{3+}$  ( $x = 0-0.08$ ). The standard card (No. PDF#01-075-8478) and all of the diffraction peaks match perfectly, which demonstrates that the LMS crystal structure is unaffected by the doped ions. The main peak at  $2\theta$  angles from  $31.0$  to  $32.0^\circ$  shifts to a low angle first and then to a high angle as a function of the  $\text{Bi}^{3+}$  doping concentration. According to Bragg's diffraction Formula (1) [16,17]:

$$2d \sin \theta = n\lambda \quad (1)$$

where  $d$  is the atomic plane spacing,  $\lambda$  is the wavelength of the incident ray,  $\theta$  represents the half diffraction angle, and  $n$  is an integer. When  $\text{Bi}^{3+}$  ( $r = 1.03 \text{ \AA}$ , CN = 6) with a larger ionic radius occupies  $\text{Mg}^{2+}$  ( $r = 0.72 \text{ \AA}$ , CN = 6) and  $\text{Sn}^{4+}$  ( $r = 0.69 \text{ \AA}$ , CN = 6) with smaller ionic radius, the lattice expands and the cell volume increases, resulting in the main diffraction peak move to a smaller angle. Although  $\text{Bi}^{3+}$  often exists in three coordination environments of five, six, and eight, the occupancy of seven-coordination of  $\text{Bi}^{3+}$  has also been reported [18]. Therefore, when  $\text{Bi}^{3+}$  is doped at a concentration of less than 0.02 mol,  $\text{Bi}^{3+}$  mainly occupies the sites of  $\text{Mg}^{2+}$  and  $\text{Sn}^{4+}$ , but La is slightly replaced and forms the third luminescent center. When the concentration of  $\text{Bi}^{3+}$  is more than 0.2 mol, the smaller  $\text{Bi}^{3+}$  mainly replaces the larger  $\text{La}^{3+}$  site [14],  $\text{Mg}^{2+}$  and  $\text{Sn}^{4+}$  are slightly replaced by  $\text{Bi}^{3+}$ , which leads to lattice shrinkage and volume reduction, and a small shift to a high angle occurs in the diffraction peak. The above results are all attributed to the abundant sites of the LMS environment. Figure 3 depicts the particle morphology and elemental mapping images, illustrating that La, Mg, Sn, O, Bi, and Sm are uniformly distributed in the LMS:  $0.02\text{Bi}^{3+}, 0.05\text{Sm}^{3+}$  sample and further demonstrating the successful incorporation of the doped ions. For perovskite-structured crystals, the lattice distortion can be characterized by the tolerance factor  $T_f$ . The closer  $T_f$  is to the value 1, the closer it is to the ideal cubic structure, indicating that the structure is the most stable and the distortion

is the smallest [19–22], which is most conducive to the formation of effective and stable luminescent centers for activator ions. The following is the calculation Formula (2) [22]:

$$T_f = \frac{R_A + R_O}{\sqrt{2} \left( \frac{R_B + R_{B'}}{2} + R_O \right)} \quad (2)$$

where  $R_A$ ,  $R_B$ ,  $R_{B'}$ , and  $R_O$  represent the ionic radius of each ion of the  $A_2BB'O_6$  perovskite-type ( $R_O = 1.4 \text{ \AA}$ , which is the ionic radius of  $O^{2-}$ ), respectively. The calculated  $T_f$  of the matrix is 0.8400,  $T_f < 1$ , indicating that LMS is a monoclinic phase structure. We also calculate  $T_f$  for samples doped with different concentrations of  $Bi^{3+}$ , as shown in Table S4. When the concentration of  $Bi^{3+}$  increases,  $T_f$  values are all below 1, and the absolute value of the difference from 1 also increases, indicating that the massive doping of  $Bi^{3+}$  enhanced the lattice distortion of LMS, which gradually weakened of the stability of the matrix structure and could not provide a stable luminescence site. Thus, when the amount of  $Bi^{3+}$  is more than 0.02 mol,  $Bi^{3+}$  preferentially occupies the  $La^{3+}$  site, but the number of luminescent centers remains unchanged, which were  $Mg_1O_6$ ,  $Mg_2/SnO_6$ , and  $LaO_7$ , respectively.

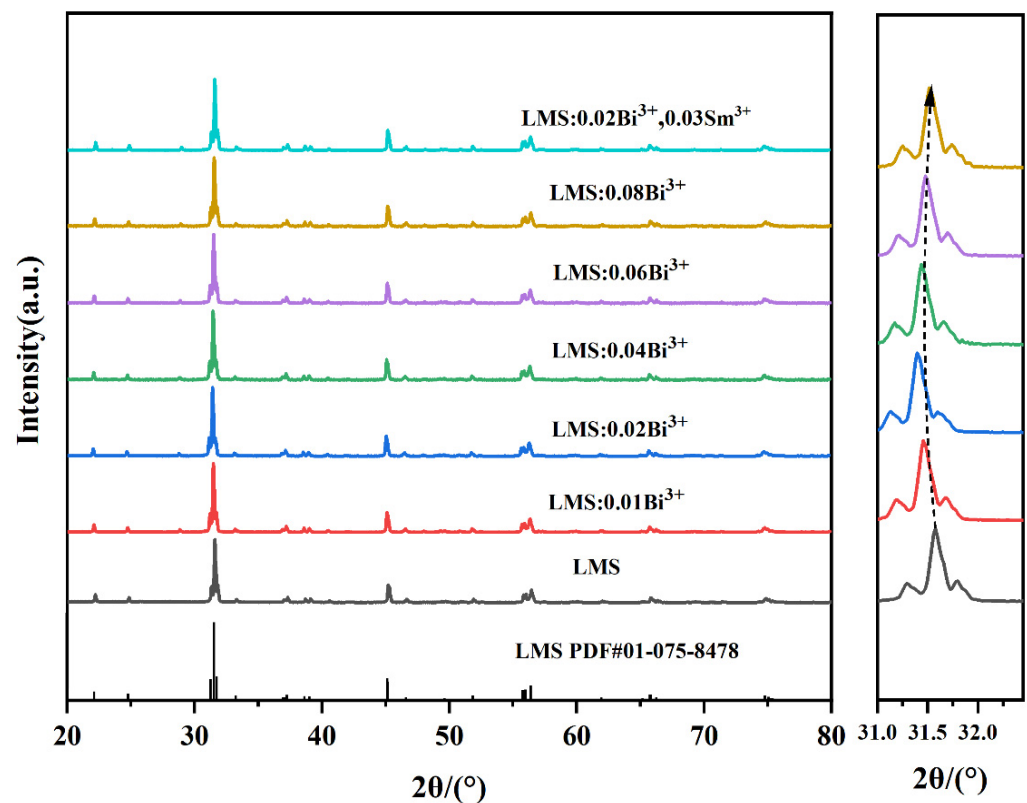


**Figure 2.** XRD pattern of LMS, LMS:  $xBi^{3+}$  ( $x = 0.01–0.08$ ), LMS: 0.02  $Bi^{3+}$ , 0.03  $Sm^{3+}$ .

Rietveld structure refinement is carried out on LMS:  $xBi^{3+}$  ( $x = 0.01–0.08$ ) with the standard card. The crystallographic information can be seen in Figure S1 and Table S1 (see Supplementary Materials). All reliability factors are all less than 10%, indicating the high reliability of the refined data. From the bond length information in Tables S2 and S3, the average bond lengths in the matrix LMS are 2.750, 2.024, and 2.240  $\text{\AA}$  for  $LaO_7$  decahedron,  $MgO_6$  octahedra, and  $SnO_6$  octahedra, respectively. When  $Bi^{3+}$  is introduced, the average bond lengths of  $LaO_7$  decahedron,  $MgO_6$  octahedra, and  $SnO_6$  octahedra in the LMS: 0.02 $Bi^{3+}$  are 2.913, 2.120, and 2.111  $\text{\AA}$ , respectively. The bond length of other ligands all slightly increase except the  $MgO_6$  octahedron, leading to the deterioration of the stability of the crystal structure and the increase of lattice distortion.

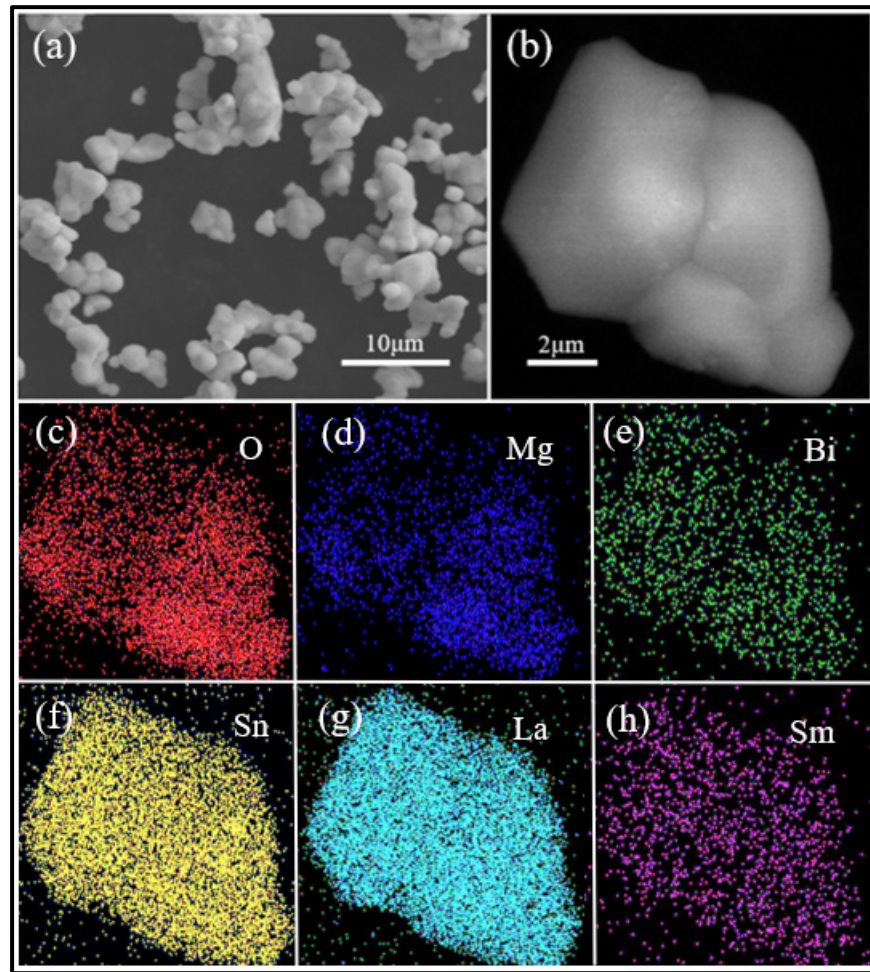


**Figure 3.** (a–h) the micromorphology and elemental mapping images of LMS: 0.02 Bi<sup>3+</sup>, 0.05 Sm<sup>3+</sup>.

To study the fluorescence characteristics of Bi<sup>3+</sup> in LMS, Figure 4a exhibits the PLE and PL spectra of LMS: 0.02Bi<sup>3+</sup>. Under the monitor at 406 nm, the PLE spectrum of Bi<sup>3+</sup> shows narrow-band excitation at 200–400 nm, and the strongest excitation wavelength is caused by the <sup>1</sup>S<sub>0</sub>→<sup>3</sup>P<sub>1</sub> transition of Bi<sup>3+</sup> at 336 nm. Broadband emission waveband from 350 to 550 nm can be seen under excitation at 336 nm, with the peak value occurring at 406 nm, covering the near ultraviolet and blue regions, which is attributed to the <sup>3</sup>P<sub>1</sub>→<sup>1</sup>S<sub>0</sub> transition of Bi<sup>3+</sup>. The wavelength of this region tends to coincide with the excitation spectrum of other activator ions, which is why Bi<sup>3+</sup> is often used as a sensitizer ion. Figure 4b exhibits the LMS: xBi<sup>3+</sup> PL spectra, the strength of the emission peak does not always increase as the Bi<sup>3+</sup> concentration rises. When the concentration of Bi<sup>3+</sup> is 0.02 mol, concentration quenching occurs, and the luminescence gradually decreases.

The critical distance between ions during concentration quenching is evaluated by Formula (3) [23]:

$$R_c = 2 \left( \frac{3V}{4\pi x_c N} \right)^{\frac{1}{3}} \quad (3)$$

where  $R_c$  represents the critical distance,  $V$  is the unit cell's volume,  $x_c$  is the critical concentration, and  $N$  represent the number of cations in a unit cell. In the LMS: 0.02Bi<sup>3+</sup> sample,  $V = 260.61 \text{ \AA}^3$ ,  $x_c = 0.02$ ,  $N = 8$ , the calculated  $R_c$  is 18.39 Å. The critical distance is greater than 5 Å, manifesting that the electric multipole interaction causes the concentration quenching of Bi<sup>3+</sup>. The Dexter Formula (4) can be used to determine the interaction type [24,25]:

$$\frac{I}{x} = \frac{k}{1 + \beta(x)^{\frac{\theta}{3}}} \quad (4)$$

where  $x$  refers to the critical concentration of  $\text{Bi}^{3+}$ ,  $I$  is the luminous intensity,  $k$  and  $\beta$  are constants, and the  $\theta$  value can define the type of interaction mechanism. Figure 4c depicts the function of  $\log(I/x)$  versus  $\log(x)$ , and the slope value is  $-1.54$ . The  $\theta$  equals 4.6, which approaches 6. Thus, dipole–dipole interaction is what causes the concentration quenching of  $\text{Bi}^{3+}$ . As given in Figure 4b, when the concentration of  $\text{Bi}^{3+}$  increases from 0.01 to 0.02, the emission spectrum of  $\text{Bi}^{3+}$  shows a redshift, which is related to the strength of the crystal field in LMS.

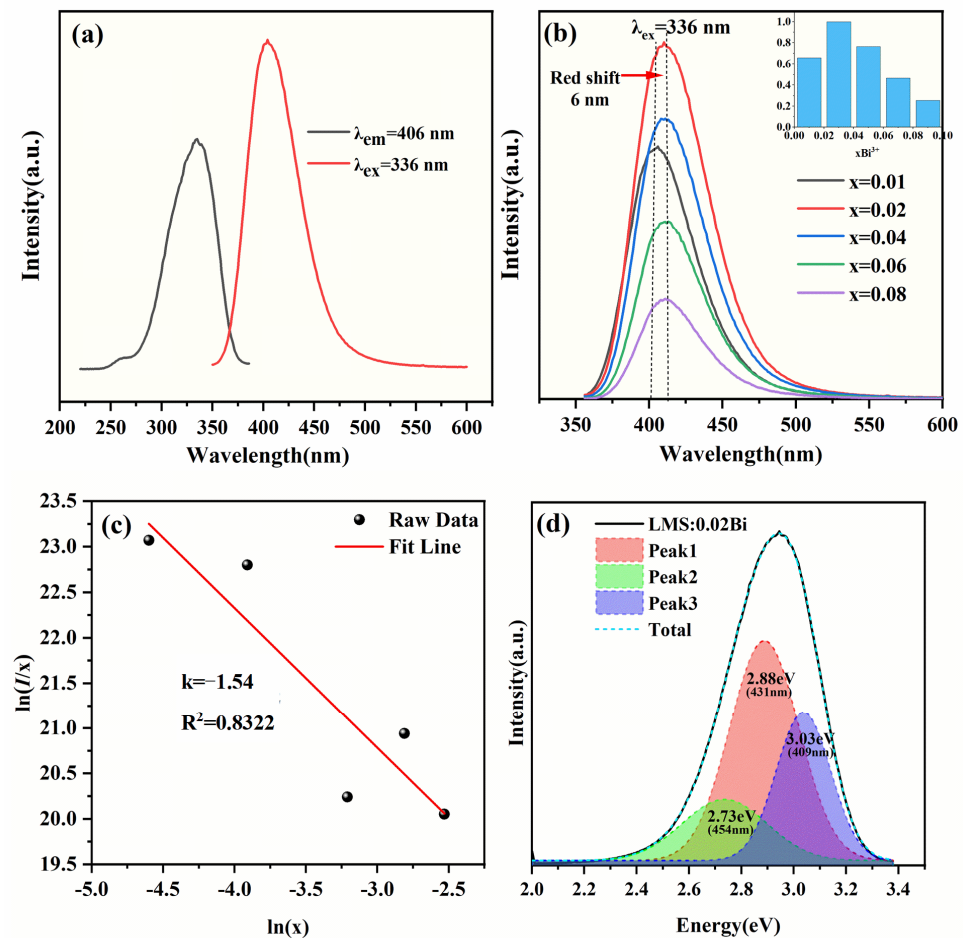


**Figure 4.** (a) PLE and PL spectra of LMS: 0.02  $\text{Bi}^{3+}$ ; (b) PL spectra of LMS:  $x\text{Bi}^{3+}$  ( $x = 0.01$ – $0.08$ ) with excitation wavelength of 336 nm; (c) concentration quenching fitting diagram of sample LMS: 0.02  $\text{Bi}^{3+}$  at 336 nm excitation; (d) Gaussian fitting diagram of LMS: 0.02  $\text{Bi}^{3+}$ .

The crystal field splitting describes the splitting between energy levels. The calculation of crystal field splitting is given by Formula (5) [26,27]:

$$D_q = \frac{1}{6} Z e^2 \frac{r^4}{R^5} \quad (5)$$

where the crystal field splitting energy is represented by  $D_q$ ,  $Z$  is the charge of anions,  $e$  is the electronic charge, the  $d$  wave function's radius is represented by  $r$ , and  $R$  is the bond length following the substitution of  $\text{Bi}^{3+}$ . When the concentration of  $\text{Bi}^{3+}$  is more than 0.02 mol, there is a red shift of 6 nm, indicating the  $\text{Bi}^{3+}$  ( $r = 1.03$  Å, CN = 6) preferentially occupies  $\text{La}^{3+}$  ( $r = 1.1$  Å, CN = 7) site. Due to the shorter bond distance of  $R_{\text{Bi-O}}$  compared to  $R_{\text{La-O}}$ , the crystal field splitting energy increases, leading to the spectral redshift. This is also evidence that the diffraction peak shift of LMS:  $x\text{Bi}^{3+}$  exhibits abnormality. As shown in Figure 4d, Gaussian fitting is performed on the emission peak of LMS: 0.02  $\text{Bi}^{3+}$ , and three emission peaks are obtained, indicating that there are three emission centers Bi1, Bi2, and Bi3 [28] during the doping process of  $\text{Bi}^{3+}$ . When  $\text{Bi}^{3+}$  enters the matrix and occupies

La<sup>3+</sup>, Mg<sup>2+</sup>, and Sn<sup>4+</sup> sites, three different emission centers are formed. Three emission centers form together a photoluminescence spectrum, which indicates that the LMS matrix can provide an excellent crystal environment for luminescent centers.

The Formula (6) presented by Van Uitert [29] can be used to calculate the Gaussian peaks corresponding to each emission center:

$$E(\text{cm}^{-1}) = Q \times \left[ 1 - \left( \frac{V}{4} \right)^{\frac{1}{V}} \times 10^{-\frac{nE_a r}{80}} \right] \quad (6)$$

where  $E$  is the activator ion's emission position,  $Q$  is the boundary of the free ionic state's lower energy position,  $V$  represents the activator ion's valence, the value  $n$  represents the coordination number of the activator ion's occupied sites,  $E_a$  is the electronic affinity of the atom forming anion, and  $r$  is the substituted ion's ionic radius. For LMS: 0.02Bi<sup>3+</sup>, the ionic radius and coordination number ( $r = 1.1 \text{ \AA}$ , CN = 7) of La<sup>3+</sup> are larger than those of Mg<sup>2+</sup> ( $r = 0.72 \text{ \AA}$ , CN = 6) and Sn<sup>4+</sup> ( $r = 0.69 \text{ \AA}$ , CN = 6). Therefore, the Bi3 emission center generated at the 409nm emission peak (3.03 eV) is caused by Bi<sup>3+</sup> occupying the La<sup>3+</sup> site, the Bi1 emission center generated at the 431 nm emission peak (2.88 eV) is caused by Bi<sup>3+</sup> occupying the Mg<sub>1</sub> site, and the Bi<sub>2</sub> emission center generated at the 454nm emission peak (2.73 eV) is caused by Bi<sup>3+</sup> occupying the Mg/Sn site.

Figure 5a depicts the PL spectra of LMS: ySm<sup>3+</sup> phosphors with different concentrations under excitation at 336 nm. The PL spectrum range covers the red region of 550–750 nm, with four distinct emission peaks located at 570, 607, 653, and 709 nm, respectively. These peaks are attributed to the electronic transitions of <sup>4</sup>G<sub>5/2</sub> → <sup>6</sup>H<sub>5/2</sub>, <sup>4</sup>G<sub>5/2</sub> → <sup>6</sup>H<sub>7/2</sub>, <sup>4</sup>G<sub>5/2</sub> → <sup>6</sup>H<sub>9/2</sub>, <sup>4</sup>G<sub>5/2</sub> → <sup>6</sup>H<sub>11/2</sub> of Sm<sup>3+</sup> [30], and the strongest excitation peak occurs at 605 nm. Concentration quenching happens at  $y = 0.05$  as Sm<sup>3+</sup> concentration rises. The PLE spectrum of LMS: 0.05 Sm<sup>3+</sup> and the PL spectrum of LMS: 0.02 Bi<sup>3+</sup> are shown in Figure 5b. It can be seen that many excitation peaks appear in the PLE spectrum range of Sm<sup>3+</sup> is 300–500 nm, which is caused by the unique energy level structure of Sm<sup>3+</sup>. The strongest excitation peak is situated near 400 nm, which overlaps greatly with the emission peak of Bi<sup>3+</sup>. Therefore, it is possible that energy will be transferred from Bi<sup>3+</sup> to Sm<sup>3+</sup> in the co-doped sample, according to preliminary findings. To further explore the link between energy transfer from Bi<sup>3+</sup> to Sm<sup>3+</sup>. Figure 5c exhibits the PL spectra of LMS: 0.02 Bi<sup>3+</sup>, ySm<sup>3+</sup> ( $y = 0.01$ – $0.11$ ) at different concentrations. Two separate distinctive peaks are visible in the 350–700 nm region. The blue emission of 350–500 nm belongs to the characteristic peak of Bi<sup>3+</sup>, and the orange-red emission of 550–700 nm ascribes to the characteristic peak of Sm<sup>3+</sup>. The results after spectral integration and normalization of the two characteristic peaks are given in Figure 5d. It is evident that when Sm<sup>3+</sup> concentration rises, the luminous intensity of Bi<sup>3+</sup> drops linearly, while the luminous intensity of Sm<sup>3+</sup> keeps rising until concentration quenching happens, indicating that under excitation at 336 nm, the energy of Bi<sup>3+</sup> is transferred to Sm<sup>3+</sup>.

The luminescent decay curves of LMS: 0.02 Bi<sup>3+</sup>, ySm<sup>3+</sup> ( $y = 0$ – $0.09$ ) are measured under excitation at 336 nm in order to further study the energy transfer relationship from Bi<sup>3+</sup> to Sm<sup>3+</sup>, as shown in Figure 6a–g. The fluorescence decay curves are fitted using the double exponential Formula (7) [31]:

$$I(t) = A_1 \exp\left(-\frac{t}{\tau_1}\right) + A_2 \exp\left(-\frac{t}{\tau_2}\right) \quad (7)$$

where the luminescent intensity of LMS: 0.02 Bi<sup>3+</sup>, ySm<sup>3+</sup> is represented by  $I(t)$  at time  $t$ ,  $A_1$  and  $A_2$  are fitting constants, and the lifetimes for quick and slow decays are  $\tau_1$  and  $\tau_2$ , respectively. Then, the average luminescent lifetime is determined by Formula (8) [32]:

$$\tau = \frac{A_1 \tau_1^2 + A_2 \tau_2^2}{A_1 \tau_1 + A_2 \tau_2} \quad (8)$$

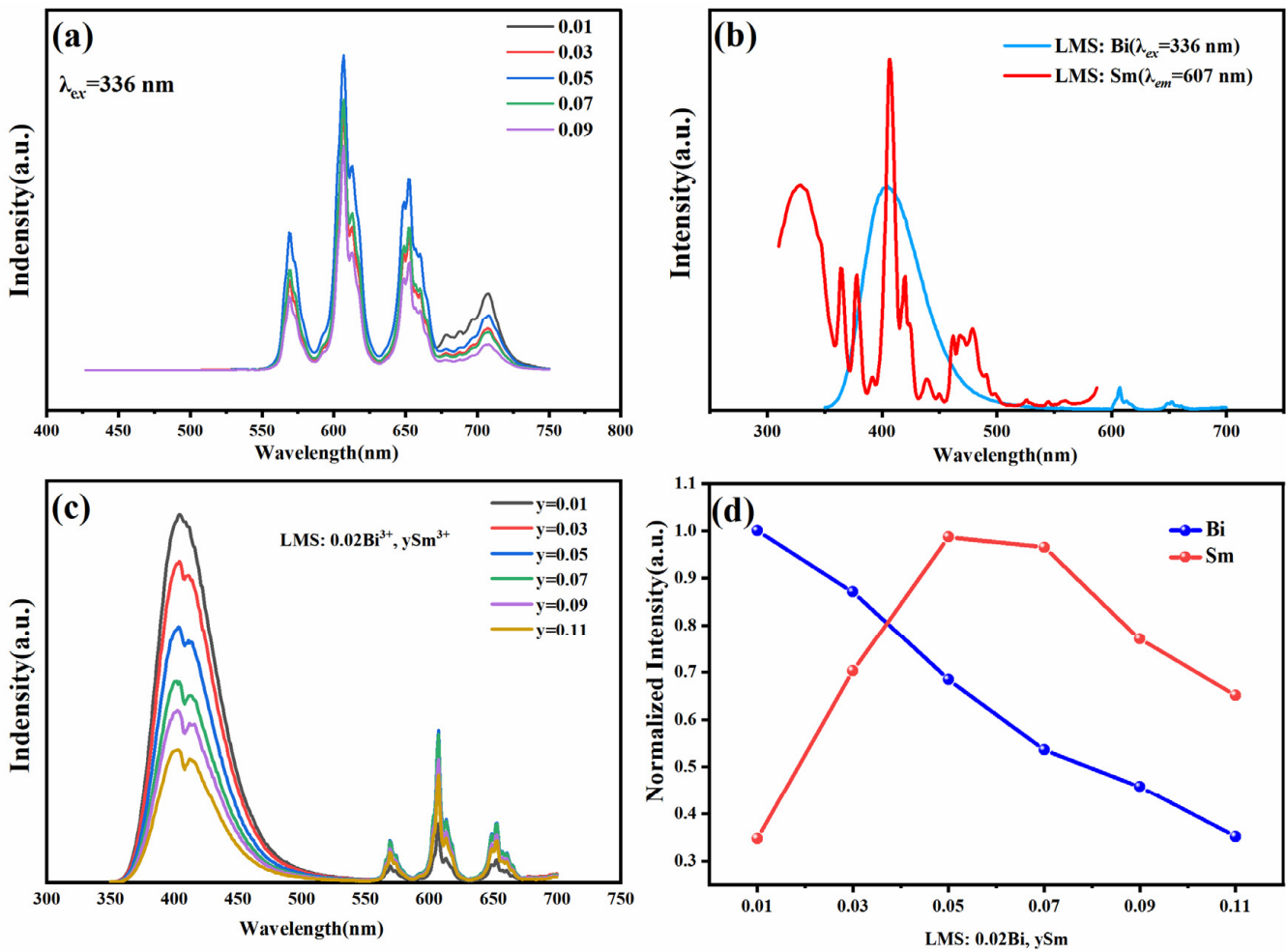


**Figure 5.** (a) LMS: ySm<sup>3+</sup> (y = 0.01–0.09) PL spectrum; (b) PL spectra of LMS: 0.02 Bi<sup>3+</sup> and PLE spectra of LMS: 0.05 Sm<sup>3+</sup>; (c) LMS: 0.02Bi<sup>3+</sup>, ySm<sup>3+</sup> (y = 0.01–0.11) PL spectrum of phosphors at 336 nm; (d) intensity variations of Bi<sup>3+</sup> and Sm<sup>3+</sup> characteristic peaks.

The luminescence center lifetime of Bi<sup>3+</sup> decays from 140 to 61.41 ns with a minimum lifetime of 57.29 ns as the concentration of Sm<sup>3+</sup> rises, indicating the indeed energy transfer from Bi<sup>3+</sup> to Sm<sup>3+</sup>. As shown in Figure 6g, when the concentration of Sm<sup>3+</sup> is higher than 0.03mol, the lifetime tends to be flat, which is related to the quenching of concentration. The presence of concentration quenching affects the energy transfer efficiency between sensitizer ions and activator ions. The energy transfer efficiency can be determined by Formula (9) [33]:

$$\eta_T = 1 - \frac{\tau}{\tau_0} \quad (9)$$

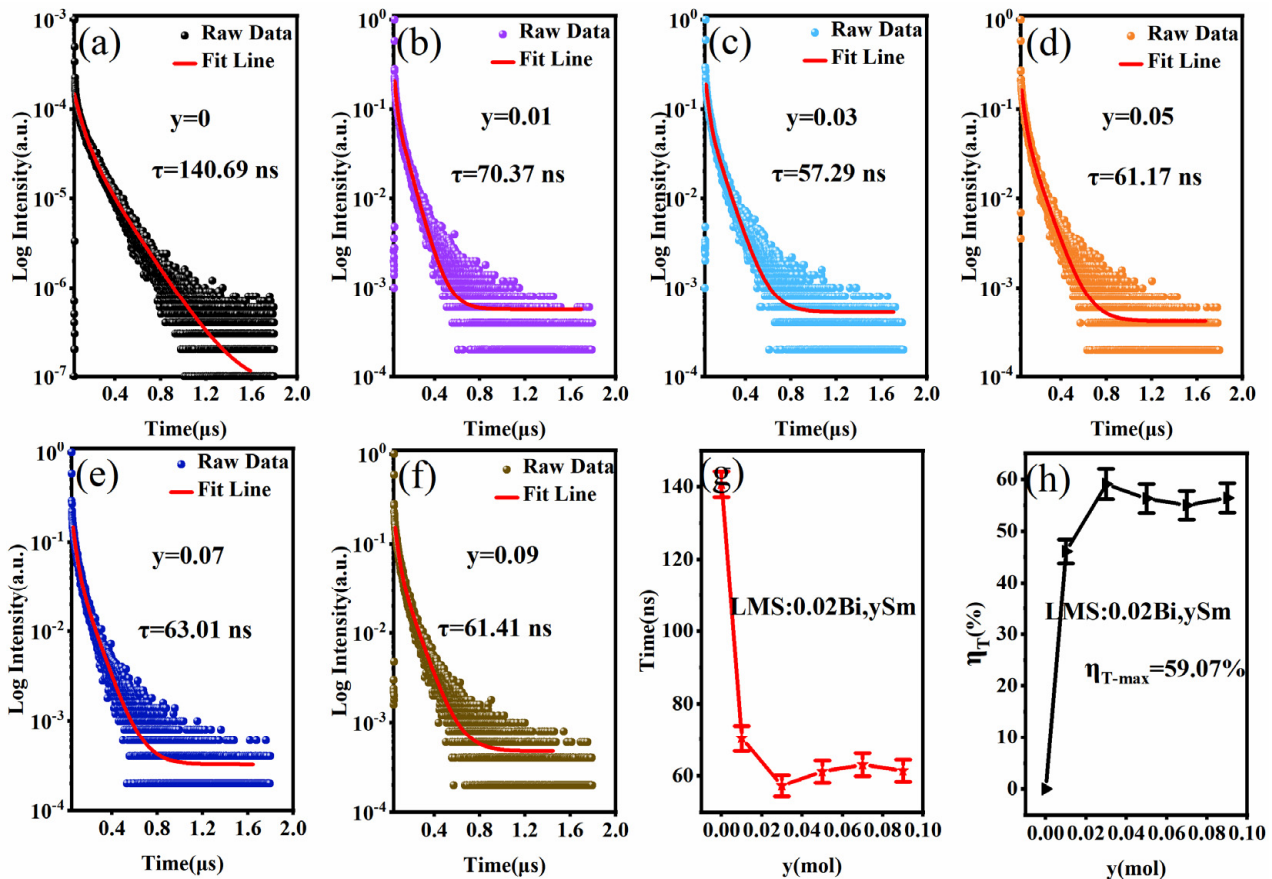
where  $\eta_T$  represents the energy transfer efficiency between sensitizer ions and activator ions, and  $\tau$  and  $\tau_0$  are the lifetime of Bi<sup>3+</sup> doped and without doped Sm<sup>3+</sup>, respectively. The calculated efficiency diagram is shown in Figure 6h, with the increase of Sm<sup>3+</sup> doping concentration, the energy transfer efficiency gradually rises and stabilizes as Sm<sup>3+</sup> doping concentration rises. These all verify the efficient energy transfer between Bi<sup>3+</sup> and Sm<sup>3+</sup>.

Figure 7a displays the thermal stability of LMS: 0.02 Bi<sup>3+</sup>, 0.05 Sm<sup>3+</sup> phosphor excited at 336 nm. All emission peaks decrease to varying degrees as the temperature increases from 303 to 503 K. The luminous intensity of Bi<sup>3+</sup> at 406 nm decays to 41.5% at 403 K, while Sm<sup>3+</sup> at 607 nm attenuates to only 59.6% of the initial temperature (303 K). The inset figure

displays that  $\text{Bi}^{3+}$  has worse thermal stability  $\text{Sm}^{3+}$ . The activation energy of phosphors can be determined using the Arrhenius Formula (10) [34,35]:

$$I_T = \frac{I_0}{1 + A \exp\left(\frac{-\Delta E}{kT}\right)} \quad (10)$$

where the luminous intensity at  $T$  temperature is characterized by  $I_T$ , the initial luminescence intensity is represented by  $I_0$ ,  $A$  is a constant, and  $k$  is the Boltzmann constant, the activation energy is determined by  $\Delta E$ . The relationship between  $\ln(I_T/I_0 - 1)$  and  $1/kT$  is plotted in Figure 7b, with the  $\Delta E$  being represented by the negative slope. The  $\Delta E$  of  $\text{Sm}^{3+}$  is 0.29 eV, while the  $\Delta E$  of  $\text{Bi}^{3+}$  is 0.21 eV. Usually, the thermal stability and activation energy of phosphors are positively connected. Therefore, the luminous intensity of  $\text{Sm}^{3+}$  is less affected by temperature than  $\text{Bi}^{3+}$ . The luminescence of  $\text{Bi}^{3+}$  is greatly affected by temperature, besides being related to its low activation energy, and the most essential reason is that  $\text{Bi}^{3+}$  luminescence is based on the transition of electron configurations of  $6s^2$  and  $6s^1 6p^1$ . This electron configuration has no outer barrier and electrons are exposed outside, and the transition is easily affected by the surrounding environment, such as coordination number, temperature, etc. However, the electronic configuration of  $\text{Sm}^{3+}$  belongs to  $4f^n$ , and the luminescence of this ion has unique characteristics, such as narrow emission peaks, long fluorescence lifetime, and difficult movement of emission peaks. These characteristics are mainly attributed to the stable transition environment created by the shielding of  $\text{Sm}^{3+}$  with 5d and 6s orbitals [13]. Figure 7c shows the variation of luminescence intensity of LMS: 0.02  $\text{Bi}^{3+}$ , 0.05  $\text{Sm}^{3+}$  from 303 to 503 K. The total luminescence intensity decreases by 49.8% when the temperature is 403 K, indicating good thermal stability of the phosphor.



**Figure 6.** (a–f) Decay curve of LMS: 0.02  $\text{Bi}^{3+}$ ,  $y\text{Sm}^{3+}$  ( $y = 0\text{--}0.09$ ) phosphors ( $\lambda_{\text{ex}} = 336$  nm); (g) the average fluorescence lifetime diagram corresponding to  $\text{Sm}^{3+}$  concentration; (h) energy transfer efficiency diagram corresponding to  $\text{Sm}^{3+}$  concentration.

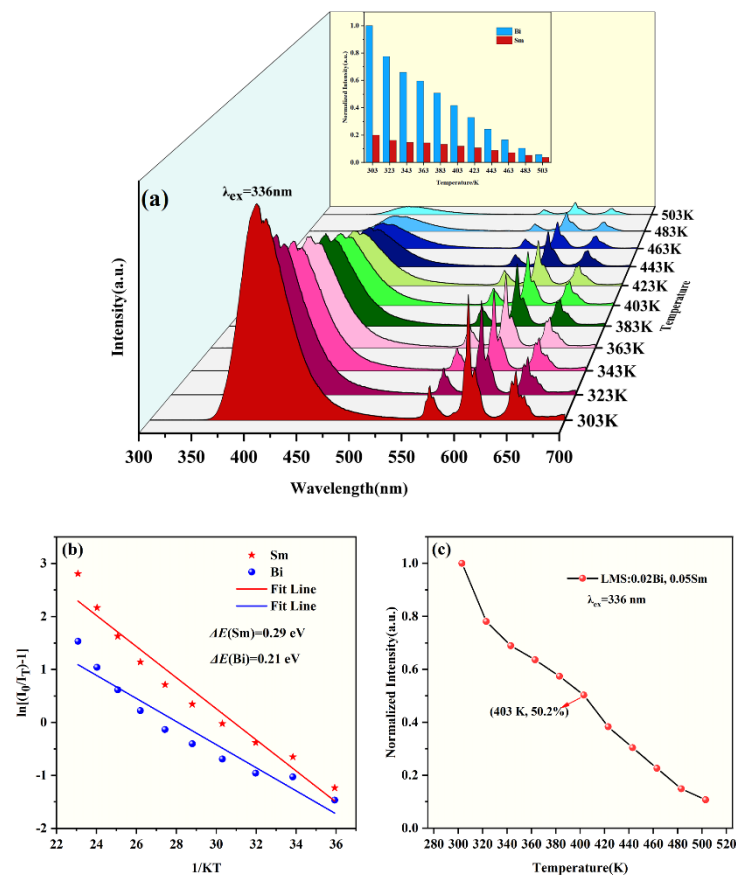


**Figure 7.** (a) Thermal stability diagram LMS: 0.02 Bi<sup>3+</sup>, 0.05 Sm<sup>3+</sup> phosphor and the change of normalized intensity of Bi<sup>3+</sup> and Sm<sup>3+</sup> (inset); (b) fitting diagram of activation energy of LMS: 0.02 Bi<sup>3+</sup>, 0.05 Sm<sup>3+</sup> phosphor; (c) luminous intensity variation of LMS: 0.02 Bi<sup>3+</sup>, 0.05 Sm<sup>3+</sup> phosphor with different temperature.

The difference of fluorescence thermal stabilities of Bi<sup>3+</sup> and Sm<sup>3+</sup> have a specific nonlinear relationship with temperature. Many literatures have reported to the realization of temperature sensors based on the thermal stability differences of these two ions [36,37], which makes it possible for LMS: 0.02 Bi<sup>3+</sup>, 0.05 Sm<sup>3+</sup> phosphor to be used in optical temperature sensors. The ratio of the luminescent intensity of Bi<sup>3+</sup> to Sm<sup>3+</sup> is defined as FIR (fluorescence intensity ratio), which can be converted from the above Formula (10) to the following Formula (11) [38]:

$$FIR = \frac{I_{Sm}}{I_{Bi}} = \frac{I_{(0,Sm)}}{I_{(0,Bi)}} \frac{1 + A_{Bi} \exp\left(-\frac{\Delta E_{Bi}}{kT}\right)}{1 + A_{Sm} \exp\left(-\frac{\Delta E_{Sm}}{kT}\right)} \approx B + C \exp\left(-\frac{\Delta E}{kT}\right) \quad (11)$$

where  $I(0, Sm)$  and  $I(0, Bi)$  represent the luminescent intensity of the initial temperature (303 K) of Sm<sup>3+</sup> and Bi<sup>3+</sup> at the  $T$  temperature.  $B$ ,  $C$ , and  $\Delta E$  are all fitted parameters. The fitting results are shown in Figure 8a, the fitting variance is 99.70%, indicating that the fitting parameters are highly credible. In addition, the FIR increases exponentially from 0.198 to 0.610 with the increase of temperature from 303 to 503 K. The performance of optical temperature sensors is characterized by absolute sensitivity  $S_a$  and relative sensitivity  $S_r$ , which can be characterized using the following formulas [39,40]:

$$S_a = \left| \frac{\partial FIR}{\partial T} \right| = C \exp\left(-\frac{\Delta E}{kT}\right) \times \frac{\Delta E}{kT^2} \quad (12)$$

$$S_r = \left| \frac{\partial FIR}{\partial T} \frac{1}{FIR} \right| \times 100\% = \frac{C \exp\left(-\frac{\Delta E}{kT}\right)}{B + C \exp\left(-\frac{\Delta E}{kT}\right)} \times \frac{\Delta E}{kT^2} \quad (13)$$

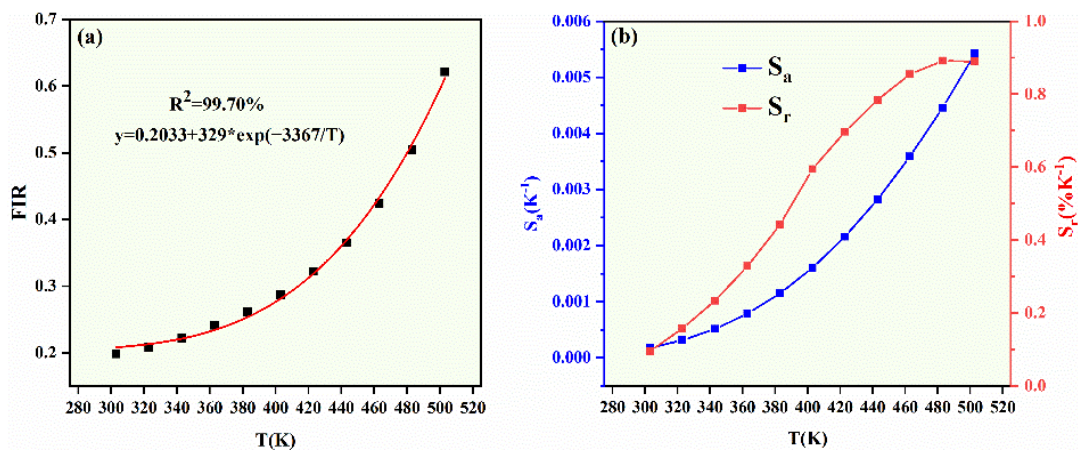


**Figure 8.** (a) FIR fitting diagram of LMS: 0.02 Bi<sup>3+</sup>, 0.05 Sm<sup>3+</sup> phosphor; (b) absolute sensitivity  $S_a$  and relative sensitivity  $S_r$  diagram of LMS: 0.02 Bi<sup>3+</sup>, 0.05 Sm<sup>3+</sup> phosphor as optical temperature sensors.

The above two formulas show that both  $S_a$  and  $S_r$  are related to FIR. As shown in Figure 8b, both sensitivities present an upward trend as the temperature rises. The maximum value of  $S_a$  and  $S_r$  are 0.0055 and 0.88%  $K^{-1}$  at 503 K, respectively.

Table 2 compares the sensitivity of phosphors used as optical temperature sensors with previous results. Obviously, the LMS: 0.02Bi<sup>3+</sup>, 0.05Sm<sup>3+</sup> phosphor have a slight advantage in absolute sensitivity and a more pronounced advantage in relative sensitivity. These all indicate that the potential application of LMS: 0.02Bi<sup>3+</sup>, 0.05Sm<sup>3+</sup> phosphor in optical temperature sensors.

**Table 2.** Comparison of sensitivity between LMS: 0.02Bi<sup>3+</sup>, 0.05Sm<sup>3+</sup> phosphor, and other phosphors as optical temperature sensors.

Compounds	Temperature Range (K)	$S_a$ -max ( $K^{-1}$ )	$S_r$ -max ( $\%K^{-1}$ )	Ref
BaY <sub>2</sub> F <sub>8</sub> :Yb <sup>3+</sup> /Ho <sup>3+</sup>	330–425	0.0057	0.6051	[41]
Y <sub>2</sub> O <sub>3</sub> : Tb <sup>3+</sup> /Eu <sup>3+</sup>	313–513	0.0261	0.683	[42]
LiY <sub>9</sub> (SiO <sub>4</sub> ) <sub>6</sub> O <sub>2</sub> : Ce <sup>3+</sup> /Dy <sup>3+</sup>	300–400	—	0.43	[43]
La <sub>2</sub> ZnTiO <sub>6</sub> : Bi <sup>3+</sup> /Eu <sup>3+</sup>	293–573	0.0032	1.23	[44]
NaYTiO <sub>4</sub> : Yb <sup>3+</sup> /Er <sup>3+</sup>	308–618	0.0045	—	[45]
Ca <sub>2</sub> MgWO <sub>6</sub> : Er <sup>3+</sup> /Yb <sup>3+</sup>	303–573	0.126	0.11	[46]
La <sub>2</sub> MgSnO <sub>6</sub> : Bi <sup>3+</sup> /Sm <sup>3+</sup>	303–503	0.0055	0.88	This work

#### 4. Conclusions

The conventional high-temperature solid-state approach was used to synthesize the LMS: xBi<sup>3+</sup> ( $x = 0.01$ – $0.08$ ) and LMS: 0.02 Bi<sup>3+</sup>, ySm<sup>3+</sup> ( $y = 0.01$ – $0.11$ ) phosphors. The refined data exhibits that the main peak of the XRD spectrum changes irregularly with a rise in Bi<sup>3+</sup> concentration. The optimal emission concentration for Bi<sup>3+</sup> is 0.02 mol. when the concentration of Bi<sup>3+</sup> exceeds 0.2 mol, the emission spectrum is red-shifted. The three luminescence centers of Bi<sup>3+</sup> were demonstrated using Gaussian fitting and Van Unitert's formula. By analyzing fluorescent spectra and luminescent decay curves, the mechanism and efficiency of energy transfer from Bi<sup>3+</sup> to Sm<sup>3+</sup> were validated and computed. The maximum efficiency of energy transfer is 59.07%. In terms of thermal stability, the emission intensity remains 50.2% of the initial intensity at 403K. Finally, the optimal values for the relative and absolute sensitivity were obtained by fitting the FIR fluorescence index at 503 K, with 0.0055  $K^{-1}$  and 0.88%  $K^{-1}$ , respectively. These results demonstrate that LMS: Bi<sup>3+</sup>, Sm<sup>3+</sup> phosphor is a promising candidate material for optical thermometry.

**Supplementary Materials:** The following supporting information can be downloaded at: <https://www.mdpi.com/article/10.3390/cryst13070991/s1>, Figure S1: (a)–(e) Refined maps of LMS:  $x\text{Bi}^{3+}$  ( $x = 0.01–0.08$ ), respectively; (f) variation in cell volume; Table S1: Cell parameters and refinement data of LMS:  $x\text{Bi}^{3+}$  ( $x = 0.01–0.08$ ); Table S2: Cation bond length information in matrix LMS; Table S3: Cation bond length information in LMS:  $0.02\text{Bi}^{3+}$ ; Table S4: “Tolerance factor” of LMS:  $x\text{Bi}^{3+}$ .

**Author Contributions:** Conceptualization, Q.X. and X.C.; methodology, Q.X.; software, X.C.; validation, W.Q.; formal analysis, Q.X.; investigation, K.S.; resources, Q.X.; data curation, Q.X.; writing—original draft preparation, Q.X.; writing—review and editing, K.S., X.Y. and R.M.; visualization, Q.X.; supervision, K.S.; project administration, K.S.; funding acquisition, K.S. All authors have read and agreed to the published version of the manuscript.

**Funding:** This research was funded by the National Natural Science Foundation of China under Grant No.: 51672063, 52161145401 and the Guangdong Key Platform & Programs of the Education Department of Guangdong Province for funding under Grant No. 2021ZDZX1003.

**Institutional Review Board Statement:** Not applicable.

**Informed Consent Statement:** Not applicable.

**Data Availability Statement:** Not applicable.

**Conflicts of Interest:** The authors declare no conflict of interest.

## References

1. Zhong, L.; Jiang, S.; Wang, X.; Li, Y.; Wang, Y.; Xie, J.; Ling, F.; Wang, Y.; Xiang, G.; Li, L.; et al. Dual-mode optical thermometry based on intervalence charge transfer excitations in  $\text{Tb}^{3+}/\text{Pr}^{3+}$  co-doped  $\text{CaNb}_2\text{O}_6$  phosphors. *Ceram. Int.* **2022**, *48*, 30005–30011. [[CrossRef](#)]
2. Su, Y.; Yuan, L.; Liu, H.; Xiong, G.; Wu, H.; Hu, Y.; Cheng, X.; Jin, Y. Multi-site occupation of  $\text{Cr}^{3+}$  toward developing broadband near-infrared phosphors. *Ceram. Int.* **2021**, *47*, 23558–23563. [[CrossRef](#)]
3. Guo, J.; Guo, J.; Gao, J.; Chen, J.; Yang, Y.; Yang, Y.; Zheng, L.; Li, Y.; Zhao, L.; Deng, B.; et al. A novel broadband-excited  $\text{LaNb}_2\text{VO}_9$ :  $\text{Sm}^{3+}$  orange-red-emitting phosphor with zero-thermal-quenching behavior for WLEDs and personal identification. *Ceram. Int.* **2022**, *48*, 26992–27002.
4. Wang, C.; Jin, Y.; Yuan, L.; Wu, H.; Ju, G.; Li, Z.; Liu, D.; Lv, Y.; Chen, L.; Hu, Y. A spatial/temporal dual-mode optical thermometry platform based on synergetic luminescence of  $\text{Ti}^{4+}$ - $\text{Eu}^{3+}$  embedded flexible 3D micro-rod arrays: High-sensitive temperature sensing and multi-dimensional high-level secure anti-counterfeiting. *Chem. Eng. J.* **2019**, *374*, 992–1004. [[CrossRef](#)]
5. Sinha, S.; Mahata, M.K.; Swart, H.C.; Kumar, A.; Kumar, K. Enhancement of upconversion, temperature sensing and cathodoluminescence in the  $\text{K}^+/\text{Na}^+$  compensated  $\text{CaMoO}_4$ :  $\text{Er}^{3+}/\text{Yb}^{3+}$  nanophosphor. *New J. Chem.* **2017**, *41*, 5362–5372. [[CrossRef](#)]
6. Wei, R.; Guo, J.; Li, K.; Yang, L.; Tian, X.; Li, X.; Hu, F.; Guo, H. Dual-emitting  $\text{SrY}_2\text{O}_4$ :  $\text{Bi}^{3+}$ ,  $\text{Eu}^{3+}$  phosphor for ratiometric temperature sensing. *J. Lumin.* **2019**, *216*, 116737. [[CrossRef](#)]
7. Pankratov, V.; Popov, A.I.; Chernov, S.A.; Zharkouskaya, A.; Feldmann, C. Mechanism for energy transfer processes between  $\text{Ce}^{3+}$  and  $\text{Tb}^{3+}$  in  $\text{LaPO}_4$ : Ce, Tb nanocrystals by time-resolved luminescence spectroscopy. *Phys. Status Solidi B* **2010**, *247*, 2252–2257. [[CrossRef](#)]
8. Van Wijngaarden, J.; Scheidelaar, S.; Vlugt, T.; Reid, M.; Meijerink, A. Energy transfer mechanism for downconversion in the ( $\text{Pr}^{3+}$ ,  $\text{Yb}^{3+}$ ) couple. *Phys. Rev. B* **2010**, *81*, 155112. [[CrossRef](#)]
9. Su, B.; Xie, H.; Tan, Y.; Zhao, Y.; Yang, Q.; Zhang, S. Luminescent properties, energy transfer, and thermal stability of double perovskites  $\text{La}_2\text{MgTiO}_6$ :  $\text{Sm}^{3+}$ ,  $\text{Eu}^{3+}$ . *J. Lumin.* **2018**, *204*, 457–463. [[CrossRef](#)]
10. Gao, P.; Dong, P.; Zhou, Z.; Li, Q.; Li, H.; Zhou, Z.; Xia, M.; Zhang, P. Enhanced luminescence and energy transfer performance of double perovskite structure  $\text{Gd}_2\text{MgTiO}_6$ :  $\text{Bi}^{3+}$ ,  $\text{Mn}^{4+}$  phosphor for indoor plant growth LED lighting. *Ceram. Int.* **2021**, *47*, 16588–16596. [[CrossRef](#)]
11. Ji, C.; Huang, Z.; Wen, J.; Zhang, J.; Tian, X.; He, H.; Zhang, L.; Huang, T.-H.; Xie, W.; Peng, Y. Blue-emitting Bi-doped double perovskite  $\text{Gd}_2\text{ZnTiO}_6$  phosphor with near-ultraviolet excitation for warm white light-emitting diodes. *J. Alloys Compd.* **2019**, *788*, 1127–1136. [[CrossRef](#)]
12. Cai, P.; Qin, L.; Chen, C.; Wang, J.; Bi, S.; Kim, S.I.; Huang, Y.; Seo, H.J. Optical thermometry based on vibration sidebands in  $\text{Y}_2\text{MgTiO}_6$ :  $\text{Mn}^{4+}$  double perovskite. *Inorg. Chem.* **2018**, *57*, 3073–3081. [[CrossRef](#)] [[PubMed](#)]
13. Wang, Q.; Mu, Z.; Zhang, S.; Du, Q.; Qian, Y.; Zhu, D.; Wu, F.  $\text{Bi}^{3+}$  and  $\text{Sm}^{3+}$  co-doped  $\text{La}_2\text{MgGeO}_6$ : A novel color-temperature indicator based on different heat quenching behavior from different luminescent centers. *J. Lumin.* **2019**, *206*, 462–468. [[CrossRef](#)]
14. Lu, Z.; Sun, D.; Lyu, Z.; Shen, S.; Wang, J.; Zhao, H.; Wang, L.; You, H. Double Perovskite  $\text{Mn}^{4+}$ -Doped  $\text{La}_2\text{CaSnO}_6/\text{La}_2\text{MgSnO}_6$  Phosphor for Near-Ultraviolet Light Excited W-LEDs and Plant Growth. *Molecules* **2022**, *27*, 7697. [[CrossRef](#)]

15. Wu, Q.; Li, P.; Ye, Z.; Huo, X.; Yang, H.; Wang, Y.; Wang, D.; Zhao, J.; Yang, Z.; Wang, Z. Near-infrared emitting phosphor  $\text{LaMg}_{0.5}(\text{SnGe})_{0.5}\text{O}_3: \text{Cr}^{3+}$  for plant growth applications: Crystal structure, luminescence, and thermal stability. *Inorg. Chem.* **2021**, *60*, 16593–16603. [[CrossRef](#)] [[PubMed](#)]
16. Fu, A.; Guan, A.; Yu, D.; Xia, S.; Gao, F.; Zhang, X.; Zhou, L.; Li, Y.; Li, R. Synthesis, structure, and luminescence properties of a novel double-perovskite  $\text{Sr}_2\text{LaNbO}_6: \text{Mn}^{4+}$  phosphor. *Mater. Res. Bull.* **2017**, *88*, 258–265. [[CrossRef](#)]
17. Bragg, W.H.; Bragg, W.L. The reflection of X-rays by crystals. *Proc. R. Soc. Lond. Ser. A Contain. Pap. Math. Phys. Character* **1913**, *88*, 428–438. [[CrossRef](#)]
18. Jaffar, B.M.; Swart, H.C.; Seed Ahmed, H.A.A.; Yousif, A.; Kroon, R.E. Luminescence properties of Bi doped  $\text{La}_2\text{O}_3$  powder phosphor. *J. Lumin.* **2019**, *209*, 217–224. [[CrossRef](#)]
19. Maughan, A.E.; Ganose, A.M.; Almaker, M.A.; Scanlon, D.O.; Neilson, J.R. Tolerance factor and cooperative tilting effects in vacancy-ordered double perovskite halides. *Chem. Mater.* **2018**, *30*, 3909–3919. [[CrossRef](#)]
20. Bartel, C.J.; Sutton, C.; Goldsmith, B.R.; Ouyang, R.; Musgrave, C.B.; Ghiringhelli, L.M.; Scheffler, M. New tolerance factor to predict the stability of perovskite oxides and halides. *Sci. Adv.* **2019**, *5*, eaav0693. [[CrossRef](#)]
21. Hanif, A.; Aldaghfag, S.; Aziz, A.; Yaseen, M.; Murtaza, A. Theoretical investigation of physical properties of  $\text{Sr}_2\text{XNbO}_6$  (X = La, Lu) double perovskite oxides for optoelectronic and thermoelectric applications. *Int. J. Energy Res.* **2022**, *46*, 10633–10643. [[CrossRef](#)]
22. Shi, C.; Yu, C.H.; Zhang, W. Predicting and screening dielectric transitions in a series of hybrid organic–inorganic double perovskites via an extended tolerance factor approach. *Angew. Chem.* **2016**, *128*, 5892–5896. [[CrossRef](#)]
23. Yun, X.; Zhou, J.; Zhu, Y.; Li, X.; Liu, S.; Xu, D. A Potentially Multifunctional Double-Perovskite  $\text{Sr}_2\text{ScTaO}_6: \text{Mn}^{4+}, \text{Eu}^{3+}$  Phosphor for Optical Temperature Sensing and Indoor Plant Growth Lighting. *J. Lumin.* **2022**, *244*, 118724. [[CrossRef](#)]
24. Dexter, D.L.; Schulman, J.H. Theory of concentration quenching in inorganic phosphors. *J. Chem. Phys.* **1954**, *22*, 1063–1070. [[CrossRef](#)]
25. Tang, H.; Zhang, X.; Cheng, L.; Mi, X.; Liu, Q. Crystal Structure, Luminescence Properties and Thermal Stability of  $\text{Lu}^{3+}$  Ion-Substituted  $\text{BaY}_2\text{Si}_3\text{O}_{10}: \text{Dy}^{3+}$  Phosphors. *J. Alloys Compd.* **2022**, *898*, 162758. [[CrossRef](#)]
26. Sun, J.F.; Lian, Z.P.; Shen, G.Q.; Shen, D.Z. Blue–white–orange color-tunable luminescence of  $\text{Ce}^{3+}/\text{Mn}^{2+}$ -codoped  $\text{NaCaBO}_3$  via energy transfer: Potential single-phase white-light-emitting phosphors. *RSC Adv.* **2013**, *3*, 18395–18405. [[CrossRef](#)]
27. Ding, X.; Zhu, G.; Geng, W.; Mikami, M.; Wang, Y. Novel blue and green phosphors obtained from  $\text{K}_2\text{ZrSi}_3\text{O}_9: \text{Eu}^{2+}$  compounds with different charge compensation ions for LEDs under near-UV excitation. *J. Mater. Chem. C* **2015**, *3*, 6676–6685. [[CrossRef](#)]
28. Zhou, H.; Wang, Q.; Jin, Y. Temperature dependence of energy transfer in tunable white light-emitting phosphor  $\text{BaY}_2\text{Si}_3\text{O}_{10}: \text{Bi}^{3+}, \text{Eu}^{3+}$  for near UV LEDs. *J. Mater. Chem. C* **2015**, *3*, 11151–11162. [[CrossRef](#)]
29. Van Uitert, L.G. An empirical relation fitting the position in energy of the lower d-band edge for  $\text{Eu}^{2+}$  or  $\text{Ce}^{3+}$  in various compounds. *J. Lumin.* **1984**, *29*, 1–9. [[CrossRef](#)]
30. Tang, T.P.; Lee, C.M.; Yen, F.C. The photoluminescence of  $\text{SrAl}_2\text{O}_4: \text{Sm}$  phosphors. *Ceram. Int.* **2006**, *32*, 665–671. [[CrossRef](#)]
31. Walfort, B.; Gartmann, N.; Afshani, J.; Rosspeintner, A.; Hagemann, H. Effect of excitation wavelength (blue vs near UV) and dopant concentrations on afterglow and fast decay of persistent phosphor  $\text{SrAl}_2\text{O}_4: \text{Eu}^{2+}, \text{Dy}^{3+}$ . *J. Rare Earths* **2022**, *40*, 1022–1028. [[CrossRef](#)]
32. Adachi, S. Temperature Dependence of Luminescence Intensity and Decay Time in  $\text{Mn}^{4+}$ -Activated Oxide Phosphors. *ECS J. Solid State Sci. Technol.* **2022**, *11*, 056003. [[CrossRef](#)]
33. Chen, H.; Wang, Y.  $\text{Sr}_2\text{LiScB}_4\text{O}_{10}: \text{Ce}^{3+}/\text{Tb}^{3+}$ : A green-emitting phosphor with high energy transfer efficiency and stability for LEDs and FEDs. *Inorg. Chem.* **2019**, *58*, 7440–7452. [[CrossRef](#)] [[PubMed](#)]
34. Fartode, S.A.; Fartode, A.P.; Dhoble, S.J. A review: Thermoluminescence dosimetric application for phosphor. *AIP Conf. Proc.* **2019**, *2104*, 020043.
35. Souadi, G.; Kaynar, U.H.; Oglakci, M.; Sonsuz, M.; Ayvacikli, M.; Topaksu, M.; Canimoglu, A.; Can, N. Thermoluminescence characteristics of a novel  $\text{Li}_2\text{MoO}_4$  phosphor: Heating rate, dose response and kinetic parameters. *Radiat. Phys. Chem.* **2022**, *194*, 110025. [[CrossRef](#)]
36. Fu, J.; Zhou, L.; Chen, Y.; Lin, J.; Ye, R.; Deng, D.; Chen, L.; Xu, S. Dual-mode optical thermometry based on  $\text{Bi}^{3+}/\text{Sm}^{3+}$  co-activated  $\text{BaGd}_2\text{O}_4$  phosphor with tunable sensitivity. *J. Alloys Compd.* **2022**, *897*, 163034. [[CrossRef](#)]
37. Tian, X.; Dou, H.; Wu, L. Non-contact thermometry with dual-activator luminescence of  $\text{Bi}^{3+}/\text{Sm}^{3+}: \text{YNbO}_4$  phosphor. *Ceram. Int.* **2020**, *46*, 10641–10646. [[CrossRef](#)]
38. Ran, W.; Sun, G.; Ma, X.; Zhang, L.; Yu, J.S.; Noh, H.M.; Choi, B.C.; Jeong, J.H.; Yan, T. Bifunctional application of  $\text{La}_3\text{BWO}_9: \text{Bi}^{3+}, \text{Sm}^{3+}$  phosphors with strong orange-red emission and sensitive temperature sensing properties. *Dalton Trans.* **2021**, *50*, 15187–15197. [[CrossRef](#)]
39. Song, M.; Zhao, W.; Xue, J.; Wang, L.; Wang, J. Color-tunable luminescence and temperature sensing properties of a single-phase dual-emitting  $\text{La}_2\text{LiSbO}_6: \text{Bi}^{3+}, \text{Sm}^{3+}$  phosphor. *J. Lumin.* **2021**, *235*, 118014. [[CrossRef](#)]
40. Song, Y.; Guo, N.; Li, J.; Ouyang, R.; Miao, Y.; Shao, B. Photoluminescence and temperature sensing of lanthanide  $\text{Eu}^{3+}$  and transition metal  $\text{Mn}^{4+}$  dual-doped antimonate phosphor through site-beneficial occupation. *Ceram. Int.* **2020**, *46*, 22164–22170. [[CrossRef](#)]

41. Swart, H.C.; Kumar, A.; Nair, G.B. BaY<sub>2</sub>F<sub>8</sub>: Yb<sup>3+</sup>, Ho<sup>3+</sup>/Tm<sup>3+</sup> Upconversion Phosphor for Optical Thermometer. In Proceedings of the 5th International Conference on Sensors and Electronic Instrumentation Advances SEIA' 2019, Tenerife (Canary Islands), Spain, 25–27 September 2019.
42. Peng, L.; Meng, Q.; Sun, W. Size dependent optical temperature sensing properties of Y<sub>2</sub>O<sub>3</sub>: Tb<sup>3+</sup>, Eu<sup>3+</sup> nanophosphors. *RSC Adv.* **2019**, *9*, 2581–2590. [[CrossRef](#)]
43. Li, J.-Y.; Hou, D.; Zhang, Y.; Li, H.; Lin, H.; Lin, Z.; Zhou, W.; Huang, R. Luminescence, energy transfer and temperature sensing property of Ce<sup>3+</sup>, Dy<sup>3+</sup> doped LiY<sub>9</sub>(SiO<sub>4</sub>)<sub>6</sub>O<sub>2</sub> phosphors. *J. Lumin.* **2019**, *213*, 184–190. [[CrossRef](#)]
44. Wang, J.; Lei, R.; Zhao, S.; Huang, F.; Deng, D.; Xu, S.; Wang, H. Color tunable Bi<sup>3+</sup>/Eu<sup>3+</sup> co-doped La<sub>2</sub>ZnTiO<sub>6</sub> double perovskite phosphor for dual-mode ratiometric optical thermometry. *J. Alloys Compd.* **2021**, *881*, 160601. [[CrossRef](#)]
45. Wang, Y.; Zuo, C.; Ma, C.; Ye, W.; Zhao, C.; Feng, Z.; Li, Y.; Wen, Z.; Wang, C.; Shen, X.; et al. Effects of Sc<sup>3+</sup> ions on local crystal structure and up-conversion luminescence of layered perovskite NaYTiO<sub>4</sub>: Yb<sup>3+</sup>/Er<sup>3+</sup>. *J. Alloys Compd.* **2021**, *876*, 160166. [[CrossRef](#)]
46. Jiang, Y.; Tong, Y.; Chen, S.; Zhang, W.; Hu, F.; Wei, R.; Guo, H. A three-mode self-referenced optical thermometry based on up-conversion luminescence of Ca<sub>2</sub>MgWO<sub>6</sub>: Er<sup>3+</sup>, Yb<sup>3+</sup> phosphors. *Chem. Eng. J.* **2021**, *413*, 127470. [[CrossRef](#)]

**Disclaimer/Publisher's Note:** The statements, opinions and data contained in all publications are solely those of the individual author(s) and contributor(s) and not of MDPI and/or the editor(s). MDPI and/or the editor(s) disclaim responsibility for any injury to people or property resulting from any ideas, methods, instructions or products referred to in the content.